

On the Hysteretic Behaviour of Dilute Polymer Solutions in Relaxation Following Extensional Flow

R. Sizaire, G. Lielens, I. Jaumain, R. Keunings and V. Legat
CESAME, Division of Applied Mechanics,
Université catholique de Louvain,
B-1348, Louvain-la-Neuve, Belgium

June 11, 1998

Abstract

The hysteretic behaviour of dilute polymer solutions in relaxation following extensional flow is studied in the framework of three distinct theoretical models. For ideal kinematics of uniaxial elongation, we show that the kinetic theory of FENE dumbbells and its FENE-L approximation present an hysteresis when plotting polymer stress versus average molecular extension. A similar behaviour is obtained for ideal extensional kinematics using a FENE-P constitutive equation with a spectrum of finite extensibility parameters. Finally, a numerical simulation of the filament stretching device shows that spatial inhomogeneities of the stress and average conformation fields also lead to hysteretic behaviour with a single-mode FENE-CR constitutive equation. In all three cases, hysteretic behaviour results from the combined effect of dispersity and non-linearity.

We also address the validity of the stress-optic law for FENE dumbbells in relaxation following start-up of uniaxial extension. The simulation results show that the stress-optic coefficient remains constant at low strains only. Plots of stress-optic coefficient versus birefringence show hysteresis as well. This rules out a modified stress-optic law for FENE dumbbells wherein the stress-optic coefficient would be a function of the second moment of the configuration distribution function alone. Finally, it is shown in the Appendix that a proper selection of the spectrum of finite extensibilities can be made so that the multi-mode FENE-P model gives essentially the same stress response as the kinetic theory of FENE dumbbells in transient uniaxial extension.

1 Introduction

The behaviour of dilute polymer solutions in extensional flows has received much attention in recent years. Most notably, a number of experimentalists have used the filament stretching rheometer advanced by Matta and Tytus [1] and Tirtaatmadja and Sridhar [2] to measure the extensional stress that develops in polymer solutions during the start-up of flow and subsequent relaxation (e.g. [3, 4, 5, 6, 7]). One of the striking features observed experimentally is the very fast decay of stress upon cessation of flow. Whether the rapid relaxation process is a viscous stress jump or a non-linear elastic phenomenon is an open question, which is difficult to address experimentally in view of the finite time to stop the flow and the finite response time of the force transducer [7]. The recent Brownian dynamics simulations of Doyle and Shaqfeh [8] for a Kramers bead-rod chain show that the stress that develops in this model during start-up of uniaxial elongation is mainly of an elastic character. Moreover, the stress growth for bead-rod chains is qualitatively well predicted by the kinetic theory of FENE dumbbells. Doyle *et al.* [9] have investigated the relaxation of dilute polymer solutions following extensional flow by means of Brownian dynamics simulations of bead-rod chains and FENE dumbbells; they also performed macroscopic computations using the FENE-PM constitutive equation. The authors found a universal relaxation curve valid for all the models investigated, that is in quantitative agreement with experimental data after stretch at large strains. The numerical predictions of Verhoef *et al.* [7], using various multi-mode constitutive equations (i.e. the Giesekus, FENE-P and Hinch models) and the FENE dumbbell kinetic theory, showed that quantitative agreement with experimental data, both in start-up and relaxation, could only be obtained over a wide range of strains with a spectrum of (uncoupled) FENE modes. In relaxation, both the FENE-P and FENE models were found to perform well.

Another important experimental observation with polystyrene-based Boger fluids [10] is that dilute polymer solutions can show hysteretic behaviour of stress versus intrinsic birefringence in relaxation following extensional flow. Hysteresis in stress versus birefringence has been predicted in the recent numerical simulations of Lielens *et al.* [11] and Doyle *et al.* [9]. The paper by Lielens *et al.* addresses one-dimensional elongational flows. It is shown, by means of stochastic simulations, that the simple FENE dumbbell kinetic model is able to predict hysteretic behaviour. In view of the closure problem [12], the FENE theory cannot be translated into an equivalent macroscopic constitutive equation. The FENE-P constitutive equation, derived on the basis of Peterlin's approximation, is unable to predict hysteretic behaviour, as it gives a one-to-one relationship between stress and average conformation. The new closure model proposed in [11], and referred to as FENE-L, does reproduce the hysteretic behaviour of the FENE model. Doyle *et al.* [9] also found a stress-conformation hysteresis in their simulations with FENE dumbbells, both with a constant or conformation-dependent drag coefficient, but not with the FENE-PM chain, again due to the pre-averaging closure approximation. Results for the bead-rod chain model also display a more sophisticated *configuration* hysteresis, which cannot be predicted by a simple

dumbbell model. The stress–birefringence hysteresis curves obtained with the bead–rod chain and FENE dumbbell models are in qualitative agreement with the experimental observations for polystyrene–based Boger fluids.

In the present paper, we further discuss the hysteretic behaviour of dilute polymer solutions in relaxation following extensional flow. We adopt as theoretical framework the kinetic theory of FENE dumbbells and related macroscopic constitutive equations. These are summarized in Section 2. We consider in Sections 3–5 three distinct situations where hysteretic behaviour is indeed predicted: (i) ideal kinematics of uniaxial elongation, with the kinetic theory of FENE dumbbells and its FENE–L approximation, (ii) ideal kinematics of uniaxial elongation, using the multi– b FENE–P model, i.e. a multi–mode FENE–P constitutive equation with a spectrum of finite extensibility parameters, and (iii) non–ideal kinematics of the filament stretching device, with a single–mode FENE–CR constitutive equation. In all three cases, hysteretic behaviour is shown to result from the combined effect of *dispersity* and *non–linearity*. This statement is further elaborated in Section 6. In the light of our simulation results, we question in Section 7 the validity of the stress–optic law for FENE dumbbells. It is shown that the stress–optic coefficient remains constant at low strains only. Plots of stress–optic coefficient versus birefringence show hysteresis as well, which rules out a modified stress–optic law for FENE dumbbells wherein the stress–optic coefficient would be a function of the second moment of the configuration distribution function alone. This agrees qualitatively both with experimental results and chain simulation studies [8, 9, 13]. Conclusions are drawn in Section 8. Finally, it is shown in the Appendix that a proper selection of the spectrum of finite extensibilities can be made so that the multi– b FENE–P model gives essentially the same stress response as FENE dumbbells in transient uniaxial extension. The multi– b FENE–P model thus appears to be an adequate constitutive equation for describing dilute solutions of polymer chains in extensional flow.

2 The FENE dumbbell model and related constitutive equations

The Warner Finitely Extensible Non–Linear Elastic (FENE) dumbbell model [14] is the most elementary non–linear kinetic model of a dilute polymer solution. Each dumbbell consists of two identical Brownian beads connected by a spring. The beads model the interaction between the polymer and the Newtonian solvent, while the spring represents the entropic restoring force that arises from holding constant the end–to–end vector of the linear polymer. The FENE theory involves a time constant $\lambda = \zeta/4H$ and a dimensionless finite extensibility parameter $b = HQ_0^2/kT$, where ζ is the friction coefficient, k is the Boltzmann constant, and T is the absolute temperature. For simplicity, we write all subsequent equations in dimensionless form. The connector vector \mathbf{Q} , the time t and the velocity gradient κ are made dimensionless with $(kT/H)^{1/2}$, λ ,

and λ^{-1} , respectively. The polymer contribution to the stress, τ_p , is made dimensionless with nkT , where n is the dumbbell number density. For notational convenience, we define

$$h(x) = \frac{1}{1 - x/b}. \quad (1)$$

For FENE dumbbells, the dimensionless connector force \mathbf{F}^c reads

$$\mathbf{F}^c(\mathbf{Q}) = h(\mathbf{Q}^2)\mathbf{Q}, \quad (2)$$

while the polymer stress is obtained using the Kramers' expression

$$\tau_p = \langle \mathbf{Q}\mathbf{F}^c(\mathbf{Q}) \rangle - \delta, \quad (3)$$

where δ is the unit tensor and the angular brackets denote the configuration space average. The kinetic theory of FENE dumbbells does not yield an equivalent constitutive equation for the polymer stress, due to the closure problem brought about by the non-linear spring law (2). In order to compute the dynamics and polymer stress of FENE dumbbells, one either solves the diffusion equation that describes the evolution of the configuration distribution function, or, as done in the present paper, one integrates the associated Itô stochastic differential equation [15]

$$d\mathbf{Q} = [\boldsymbol{\kappa} \cdot \mathbf{Q} - \frac{1}{2}\mathbf{F}^c(\mathbf{Q})] dt + d\mathbf{W}, \quad (4)$$

for a large number N_d of individual realizations $\mathbf{Q}^{(i)}$ of the stochastic process \mathbf{Q} . In eq.(4), $\boldsymbol{\kappa}$ is the velocity gradient and \mathbf{W} denotes the three-dimensional Wiener process. We solve eq.(4) by means of the predictor-corrector scheme of weak order 2 proposed by Öttinger [15] and detailed in [12]. The polymer stress, or any other macroscopic quantity of interest, is approximated by an ensemble average, namely

$$\tau_p = \frac{1}{N_d} \sum_{i=1}^{N_d} \mathbf{Q}^{(i)}\mathbf{F}^c(\mathbf{Q}^{(i)}) - \delta. \quad (5)$$

In the present paper, we also consider three macroscopic constitutive equations, namely the FENE-P, FENE-CR and FENE-L models, that are closely related to the FENE dumbbell kinetic theory. We shall also consider a particular multi-mode FENE-P equation, which we refer to as the multi- b FENE-P model. For specified kinematics, we integrate these equations by means of a fifth-order Runge-Kutta scheme with adaptive time stepping.

The FENE-P equation is derived from the FENE theory using the self-consistent pre-averaging approximation of the spring force due to Peterlin,

$$\mathbf{F}^c(\mathbf{Q}) = h(\langle \mathbf{Q}^2 \rangle) \mathbf{Q}, \quad (6)$$

This approximation solves the closure problem [14] and yields the FENE–P constitutive equation

$$\begin{cases} \frac{D\mathbf{A}}{Dt} - \boldsymbol{\kappa} \cdot \mathbf{A} - \mathbf{A} \cdot \boldsymbol{\kappa}^T = \delta - h(\text{tr}(\mathbf{A})) \mathbf{A}, \\ \tau_p = h(\text{tr}(\mathbf{A})) \mathbf{A} - \delta, \end{cases} \quad (7)$$

where \mathbf{A} is the configuration tensor $\langle \mathbf{Q}\mathbf{Q} \rangle$ and $\frac{D\cdot}{Dt}$ denotes the material time derivative. The FENE–CR model, proposed by Chilcott and Rallison [16] reads

$$\begin{cases} \frac{D\mathbf{A}}{Dt} - \boldsymbol{\kappa} \cdot \mathbf{A} - \mathbf{A} \cdot \boldsymbol{\kappa}^T = h(\text{tr}(\mathbf{A})) [\delta - \mathbf{A}], \\ \tau_p = h(\text{tr}(\mathbf{A})) [\mathbf{A} - \delta]. \end{cases} \quad (8)$$

In essence, the FENE–CR equation is a variant of the FENE–P model designed for describing constant shear viscosity Boger fluids. A detailed comparison of the FENE, FENE–P and FENE–CR models is documented in [12, 17] for rheometrical flows.

The third macroscopic model considered in this paper is the FENE–L equation proposed by Lielens et al. [11]. It is a second–order closure model derived from the FENE dumbbell theory, that involves the configuration tensor $\mathbf{A} = \langle \mathbf{Q}\mathbf{Q} \rangle$ and the scalar average $B = \langle \text{tr}(\mathbf{Q}\mathbf{Q})^2 \rangle$. The FENE–L equation takes the form

$$\begin{cases} \frac{D\mathbf{A}}{Dt} - \boldsymbol{\kappa} \cdot \mathbf{A} - \mathbf{A} \cdot \boldsymbol{\kappa}^T = \mathbf{F}(\mathbf{A}, B), \\ \frac{DB}{Dt} = G(\boldsymbol{\kappa}, \mathbf{A}, B), \\ \tau_p = -\mathbf{F}(\mathbf{A}, B). \end{cases} \quad (9)$$

Here, the symbol \mathbf{F} and G are known algebraic expressions involving $\boldsymbol{\kappa}$, \mathbf{A} and B . They are defined in [11] for unidimensional kinematics, and in [18] for general flow fields. In comparison with the FENE–P model, FENE–L is a markedly improved approximation of the FENE kinetic theory. As the FENE–P and FENE–CR models, it can also be viewed in its own right as a phenomenological macroscopic constitutive equation with material parameters to be identified in rheometrical flows.

Finally, we shall consider a particular multi–mode FENE–P constitutive equation, which we refer to as the multi– b FENE–P model. The N_m modes are assumed uncoupled, have identical time constant λ and nkT factor but different finite extensibilities b_i , $i = 1, 2, \dots, N_m$. The polymer stress τ_p is thus the sum of the contributions $\tau_p^{(i)}$ of each mode, where $\tau_p^{(i)}$ is computed by means of eq. (7), with $b = b_i$ in eq. (1). The motivation behind the multi– b FENE–P model is an attempt at modeling the spectrum of length scales that arises in the deformation of a linear macromolecule. The modes

with small values of b_i correspond to local changes in molecular conformation that involve small parts of the polymer, while those with larger values of b_i are meant to capture the more global unraveling mechanisms of the chain that take place at larger length scales.

Alternatively, the multi- b FENE-P model can be viewed as a polydisperse suspension of non-interacting FENE-P dumbbells, or simply as a valid macroscopic constitutive equation. One should note that the multi- b FENE-P model, while having the same mathematical complexity as the FENE-PM chain model proposed by Wedgewood et al. [19] (i.e. the modes are decoupled in both cases), is in fact quite different on physical grounds. Indeed, the pre-averaging approximation used to derive the FENE-PM model implies that all modes have the *same* maximum extensibility.

3 FENE-like models in uniaxial elongation

We first consider the start-up of uniaxial elongation followed by relaxation. The velocity gradient is specified to

$$\kappa(t) = We \left(H_0(t) - H_{9/We}(t) \right) \text{diag}\left(1, -\frac{1}{2}, -\frac{1}{2}\right), \quad (10)$$

where We denotes the Weissenberg number, while $H_\alpha(t)$ is the Heaviside unit step function located at $t = \alpha$. The maximum applied strain is equal to 9, and We is set to 6. Equilibrium is specified at $t = 0$, i.e. $\tau_p(0) = 0$. In this flow, the polymer stress has the form $\tau_p = \text{diag}(\tau_{p,xx}, \tau_{p,yy}, \tau_{p,zz})$ with $\tau_{p,yy} = \tau_{p,zz}$. Macroscopic observables of interest are the mean square molecular extension, $\text{tr} \langle \mathbf{Q}\mathbf{Q} \rangle$ or $\text{tr} \mathbf{A}$, and the dimensionless polymer contribution to the time-dependent elongational viscosity, $\bar{\eta}^+ = (\tau_{p,xx} - \tau_{p,yy}) / We$.

Figure 1 compares the results obtained for $\text{tr} \langle \mathbf{Q}\mathbf{Q} \rangle$ and $\bar{\eta}^+$ with the FENE, FENE-P, FENE-CR and FENE-L models. The finite extensibility parameter is set to $b = 50$. Qualitatively, all models behave in a similar fashion, i.e. significant growth of elongational viscosity and average molecular extension until a saturation state is reached, followed by a very fast relaxation process. The FENE-CR and FENE-P equations have almost identical responses, but the FENE-L model is in markedly better agreement with the FENE results. All models follow the same stress relaxation curve, which is considerably steeper than the single exponential $\exp(-t)$.

As proposed in [9, 11], it is useful to analyze the results of Fig. 1 in a different manner, namely by plotting the elongational viscosity versus the average molecular extension. The resulting curves, parameterized by the temporal variable, are shown in Fig. 2. The main point is that the FENE and FENE-L models show hysteretic behaviour, while the FENE-P and FENE-CR equations do not. The insets of Fig. 2 give further insight into the hysteretic behaviour of FENE dumbbells. We show there the distribution $\psi(|Q_x|)$ of projected dumbbell length $|Q_x|$ at selected values of time. The function $\psi(|Q_x|)$ is readily available from the FENE stochastic simulations. At time

t_1 , $\psi(|Q_x|)$ is still very close to the equilibrium distribution. During stress growth, e.g. at time t_2 , a number of dumbbells have already gathered close to maximum extension and are oriented mainly in the x direction, thus producing a narrow peak in $\psi(|Q_x|)$; these dumbbells are essentially in an equilibrium state wherein Stoke's drag acting on the beads is balanced by the connector force. The other dumbbells, however, are still to experience further stretching and orientation. They form a *thinning tail* in the distribution $\psi(|Q_x|)$. At time t_3 , a steady state has been reached; all dumbbells are oriented mainly in the x direction and have a projected length $|Q_x|$ near the maximum extension \sqrt{b} . This we call the saturation state. During relaxation, e.g. time t_4 , the peak-shaped distribution goes back to equilibrium, but following a very different route. In fact, at times t_2 and t_4 , the FENE dumbbells have identical average molecular extension, but quite different distributions of orientation and length, thus producing significantly different polymer stresses. In view of the non-linearity of the connector force, the longer dumbbells present at time t_2 contribute higher stresses than the relatively shorter ones at time t_4 . The hysteretic behaviour of the FENE model is thus due to the fact that FENE dumbbells do not reach at the same time their saturation state. In short, we have a first illustration of the proposition (non-linearity + dispersity \rightarrow hysteresis).

As seen in Fig. 2, the FENE-L closure model has kept enough of the physics of the original FENE theory to show hysteretic behaviour as well. Indeed, it is able by construction to approximate the thinning tail of the FENE distribution during stress growth [11]. The FENE-P and FENE-CR models, however, do not show hysteretic behaviour. These constitutive equations express the polymer stress as a non-linear algebraic expression of the average molecular configuration \mathbf{A} alone, as inspection of eqs. (7) and (8) reveals. A given value of average extension thus yields a single value of stress. While non-linearity is preserved, it is dispersity that has been lost due to the pre-averaging approximation.

In the sequel, we show that dispersity in the FENE-P or FENE-CR models is recovered, and so is hysteretic behaviour, by using a spectrum of finite extensibilities or when the flow is no longer spatially homogeneous.

4 The multi-b FENE-P model in uniaxial elongation

Figure 3 illustrates the response of the FENE-P model with a spectrum of finite extensibilities in start-up of uniaxial elongation followed by relaxation (cfr. eq. (10)). For the sake of illustration, we use $N_m = 20$ modes with finite extensibilities that are linearly distributed between $b_1 = 3.5$ and $b_{20} = 20000$. We plot the elongational viscosity $\bar{\eta}^+$ versus the mean square molecular extension defined as $\frac{1}{N_m} \sum_{i=1}^{N_m} \text{tr} \mathbf{A}^{(i)}$. The results are shown for $We = 4, 6$, and 8 .

The main point is that a multi- b FENE-P model does indeed show hysteretic behaviour, thus providing a second illustration of our proposition (non-linearity + dispersity \rightarrow hysteresis). As individual FENE dumbbells do, individual FENE-P modes reach their saturation level determined by b_i at different times (or strain levels) during stress growth. Note that a multi- b FENE-CR model would respond similarly.

The analogy between the FENE and multi- b FENE-P can in fact be pushed one step further. We show in the Appendix that a proper selection of the spectrum of finite extensibilities can be made so that the multi- b FENE-P results for the transient elongational viscosity are virtually those given by the FENE dumbbell kinetic theory.

Next, we turn to the response of a single-mode FENE-CR model in the filament stretching device. Here, it is the spatial inhomogeneity of the flow that will cause dispersity. Together with the non-linearity of the pre-averaged spring force, this will imply hysteretic behaviour as well.

5 The FENE-CR model in the filament stretching device

The filament stretching device is shown schematically in Fig. 4. A cylindrical sample of quiescent fluid is placed between two circular plates of radius R_0 and separated by a length L_0 . The fluid is assumed to stick at the plate walls. At time $t = 0^+$, the upper plate is set into motion in the z direction and the fluid sample is stretched. By monitoring the force $F(t)$ needed to separate the plates and the ensuing decreasing radius $R(t)$ of the fluid column at mid-distance between the plates, one wishes to estimate the transient elongational viscosity of the fluid.

As pointed out by several authors (e.g. [20, 21, 22, 23]), the boundary conditions at the plates induce a non-uniform decrease in the radius along the filament length. The fluid is indeed deformed by a transient shear flow prior to being extended. So, the filament stretching device does not yield the ideal kinematics of homogeneous, uniaxial extension considered in the previous sections. The velocity compensation technique [2] is an attempt to produce ideal kinematics at one cross-section of the filament only. It consists in continuously adapting the plate velocity $V_p(t)$ such that the mid-distance filament radius $R(t)$ decrease exponentially, i.e.

$$R(t) = R_0 \exp\left(-\frac{1}{2}\dot{\epsilon}t\right), \quad (11)$$

where $\dot{\epsilon}$ is the specified elongation rate. One should note that the constraint (11) does *not* guarantee ideal extensional kinematics (i.e. with a spatially uniform velocity gradient κ) at the mid-distance cross-section. Ignoring inertia and gravity, one can estimate the transient elongational viscosity with the formula

$$\bar{\eta}_{est}^+(\dot{\varepsilon}, t) = \frac{1}{\dot{\varepsilon}} \left(\frac{F(t)}{\pi R(t)^2} - \frac{\gamma}{R(t)} \right), \quad (12)$$

where γ is the coefficient of surface tension.

In a recent paper [21], Sizaire and Legat have described the results of a finite element simulation of the filament stretching device for a single mode FENE–CR fluid. Values of the material parameters were those identified by McKinley in steady shear of a polyisobutylene–polybutene Boger fluid (see Table 1 of [21]). We have repeated the simulations of Sizaire and Legat, the difference between the two studies being that we specify the velocity compensation technique as a boundary condition. To the set of conservation and constitutive equations, we thus add the constraint (11). Implementation details are provided in the Ph.D. thesis of Sizaire [24].

Figure 5 shows the computed transient Trouton ratio $\bar{\eta}_{est}^+/\eta_0$ as a function of the Hencky strain $\varepsilon = \dot{\varepsilon}t$, where η_0 is the solution shear viscosity at zero shear rate. For the larger value of the finite extensibility parameter ($b = 4325$, value used in [21]), the FENE–CR behaves essentially like the Oldroyd–B fluid ($b \rightarrow \infty$) and non–linearity of the spring law does not show at Hencky strains below 4. For $b = 43$, however, the apparent elongational viscosity reaches a plateau at a Hencky strain of about 2, in a manner that is qualitatively very similar to what is observed in uniaxial extension. The important difference, however, is that the stress and conformation fields are *not homogeneous* as illustrated in Fig. 6.

We plot there the zz component of the polymer stress τ_p and configuration tensor \mathbf{A} as a function of the radial coordinate, computed at mid–distance between the plates. Although the instantaneous velocity field is that of uniaxial extension at the free surface $r = R(t)$ (in view of the constraint (11)), the polymer stress and configuration tensor are not uniform over the filament cross–section during stress growth. Since the fluid elements are moving radially–inwards in that cross–section, this shows that the velocity compensation technique does not yield ideal extensional kinematics there. We find that the fluid elements near the free surface experience larger stress and average molecular extension than those near the axis of the filament, due to the fluid’s memory of non–ideal kinematics at the early stages of stretching. This is particularly so for Hencky strains between 1.5 and 1.6. It is only at Hencky strains above 2 that the polymer stress and configuration tensor become uniform at the mid–distance filament cross–section. If the upper plate is stopped then, these profiles will relax uniformly as they would after pure extension. So, in this numerical simulation, dispersity is provided by the non–homogeneity of the polymer stress and configuration tensor during stress growth, while non–linearity is brought about by the non–linear pre–averaged spring law of the FENE–CR model. Our proposition (non–linearity + dispersity \rightarrow hysteresis) leads us to expect hysteretic behaviour in this numerical experiment as well.

Hysteretic behaviour is indeed obtained in simulations of stretching followed by relaxation in the filament stretching device, using a single mode FENE–CR model. We have performed three simulations with $b = 43$ and $\dot{\varepsilon} = 1.6, 3.2, \text{ and } 4.8$. The

plate stops at a Hencky strain of 3. The average polymer stress $\langle \tau_p \rangle$ is plotted versus the average molecular extension $\langle A \rangle$ in Fig. 7. These quantities are computed at the mid-distance filament cross section as follows

$$\begin{aligned}\langle \tau_p \rangle &= \frac{1}{\pi R^2} \int_0^R \tau_{p,zz} 2\pi r dr, \\ \langle A \rangle &= \frac{1}{R} \int_0^R A_{zz} dr.\end{aligned}\tag{13}$$

(Note that $\langle A \rangle$ is a lineal average instead of the surface average $\langle \tau_p \rangle$, in order to mimic birefringence measurements). The hysteresis curves are qualitatively similar to what we have obtained in uniaxial elongation with the FENE, FENE-L and multi- b FENE-P models. They are traversed clockwise, namely the upper part of the curve corresponds to stretching while the lower part corresponds to relaxation; all relaxation curves follow a master curve. We point out that a similar response would be obtained with a one-mode FENE-P constitutive equation.

For the larger value of the finite extensibility parameter ($b = 4325$), saturation is not yet reached when the plate is stopped at a Hencky strain of 3. While the stress and average conformation fields are not spatially homogeneous in this case either, the FENE-CR fluid essentially behaves like a linear Hookean dumbbell model, and only a very minute hysteresis is obtained [24].

6 Discussion

We have illustrated the hysteretic behaviour of dilute polymer solutions in relaxation following extensional flow, in the framework of three distinct theoretical models. For ideal kinematics of uniaxial elongation, we have shown that the kinetic theory of FENE dumbbells and its FENE-L approximation present an hysteresis when plotting polymer stress versus average molecular extension. A similar behaviour is obtained for ideal extensional kinematics using a FENE-P constitutive equation with a spectrum of finite extensibility parameters. Finally, spatial inhomogeneities in the filament stretching device also lead to hysteretic behaviour with a single mode FENE-P or FENE-CR constitutive equation. In all three cases, hysteretic behaviour results from the combined effect of dispersity and non-linearity.

Indeed, let τ^{ind} and c^{ind} denote individual contributions to the stress and average molecular conformation in the direction of elongation, respectively. For FENE dumbbells, τ^{ind} is the contribution of an individual dumbbell to the polymer stress, while c^{ind} is its contribution to the average configuration. For the multi- b FENE-P model, τ^{ind} is the scaled stress contribution $\tau_p^{(i)}/b_i$ of mode $\#i$, while c^{ind} is the corresponding scaled conformation $A^{(i)}/b_i$. Finally, in the filament stretching simulation with the single mode FENE-CR model, τ^{ind} and c^{ind} are the axial components of τ_p and \mathbf{A}

computed at one particular radial location of the mid–distance filament cross–section. In all three cases, the relation $\tau^{ind} = \tau(c^{ind})$ between individual stress and conformation is provided by a non–linear stress function τ with positive concavity.

Now, the hysteretic behaviour discussed in the previous sections arises when plotting a suitably averaged stress $\langle \tau^{ind} \rangle$ versus an average conformation $\langle c^{ind} \rangle$. For FENE dumbbells, the brackets denote the configuration space average. With the multi– b FENE–P model, $\langle \tau^{ind} \rangle$ is the sum of the stresses $\tau_p^{(i)}$ while $\langle c^{ind} \rangle$ is the arithmetic mean of the configuration tensors $A^{(i)}$. In the filament stretching simulation, $\langle \tau^{ind} \rangle$ and $\langle c^{ind} \rangle$ are the spatial averages defined in eq. (13). As shown in Fig. 8, the main point is that

$$\langle \tau^{ind} \rangle = \langle \tau(c^{ind}) \rangle \geq \tau(\langle c^{ind} \rangle), \quad (14)$$

with the equality being obtained only when there is no dispersity in the individual values of c^{ind} , i.e. when all individual contributions c^{ind} are identical. During stress growth, a broad distribution of individual configurations c^{ind} develops, leading to an average stress $\langle \tau^{ind} \rangle$ that is strictly larger than $\tau(\langle c^{ind} \rangle)$. When saturation is reached, the distribution of individual configurations c^{ind} essentially reduces to a Dirac distribution, dispersity is minimal and thus $\langle \tau^{ind} \rangle \approx \tau(\langle c^{ind} \rangle)$. This property is well preserved during most of the relaxation process, thus yielding a master curve defined by the stress function τ . In view of eq. (14), the hysteresis curve is traversed clockwise.

The hysteretic behaviour illustrated in this paper raises important questions regarding the validity of the stress–optic law. In the next section, we address this issue for FENE dumbbells.

7 The stress–optic law for FENE dumbbells

Intrinsic birefringence results from the optical anisotropy of the polymer solution undergoing flow [25, 26, 27]. Its origin lies in the anisotropic polarizability of the polymer segments. For a given model of the polymer chain, and with suitable assumptions such as the additivity of segmental polarizabilities, it is possible to relate the anisotropic part of the refractive index tensor \mathbf{n} of the polymer solution to a relevant measure of average molecular conformation. The stress–optic law states that the polymer stress τ_p is related to the refractive index tensor \mathbf{n} by a simple proportionality rule

$$\mathbf{n} = C\tau_p, \quad (15)$$

where C is a constant called the stress–optic coefficient (e.g. [26, 27]). If valid, the stress–optic law provides a non–intrusive way of measuring stresses using intrinsic birefringence data. As discussed in recent papers [8, 13], it is generally acknowledged

that the stress–optic law fails under conditions of strong flow. In the present section, we discuss the validity of the stress–optic law for FENE dumbbells in the simulation of start–up of uniaxial elongation followed by relaxation.

An expression for the intrinsic birefringence for FENE dumbbells is obtained by considering the connector vector \mathbf{Q} as the end–to–end vector of a freely–jointed bead–rod chain [8, 13, 25]. In uniaxial elongation (cfr. eq. (10)), the dimensionless birefringence Δn reads

$$\Delta n = \langle Q_x Q_x \rangle - \langle Q_y Q_y \rangle. \quad (16)$$

If the stress–optic law is valid, the dimensionless stress–optic coefficient

$$C = \frac{\langle Q_x Q_x \rangle - \langle Q_y Q_y \rangle}{\tau_{p,xx} - \tau_{p,yy}} \quad (17)$$

should thus remain constant during stress growth and relaxation.

Figure 9 illustrates the temporal evolution of the stress–optic coefficient C for $We = 6$ and a maximum applied strain of 9. The calculations are for $b = 4325$. During stress growth, the stress–optic coefficient C is indeed constant at low strains, where non–linearity of the spring force does not yet intervene. At larger strains, however, C rapidly decreases due to non–linear elastic effects. During the relaxation process, the stress–optic coefficient quickly goes back to its low strain plateau value. These results invalidate the stress–optic law for FENE dumbbells. They are in qualitative agreement with the recent simulations of bead–rod [8] and FENE–P [13] chains in start–up of elongation.

It is useful to plot the stress–optic coefficient versus birefringence, as we did in Fig. 2 for stress versus conformation. This again gives an hysteresis shown in Fig. 10. So, for a given value of birefringence, a dilute polymer solution modeled by FENE dumbbells may have multiple values for the stress–optic coefficient in time–dependent strong flows. This is also in qualitative agreement with the experimental results and bead–rod chain simulations reported in [9].

Unlike for a FENE–P or FENE–CR fluid, the hysteretic behaviour of Fig. 10 rules out a modified stress–optic law for FENE dumbbells wherein the stress–optic coefficient would be a function of the second moment $\langle \mathbf{Q}\mathbf{Q} \rangle$ alone.

8 Conclusions

In the framework of kinetic theory of FENE dumbbells and related macroscopic equations, we have shown that hysteretic behaviour results from the combined effect of dispersity and non–linearity.

With FENE dumbbells, dispersity results from a coarse–grain version of molecular individualism [28]. At start–up of flow, individual dumbbells have their own configuration dictated by an equilibrium distribution, thus yielding different non–linear dynamics during stress growth. A more sophisticated version of molecular individualism

is observed in simulations with bead–spring or bead–rod chains, eventually leading to a configuration hysteresis [9, 13, 29]. Molecular individualism can also be traced in the multi- b FENE–P calculations, should one wish to interpret this model as a polydisperse suspension of FENE–P dumbbells of different maximum length. In the simulation of the filament stretching device with a single mode FENE–CR model, dispersity is not due to molecular individualism at all, but rather to the non–ideal character of the flow kinematics inducing different deformation histories across the mid–distance section of the filament. In an actual experiment with the filament stretching device, it may thus be difficult to identify the relative contributions to hysteretic behaviour of molecular individualism and flow inhomogeneities. The current development of micro–macro numerical techniques that couple stochastic simulations of kinetic theory models with the finite element solution of the conservation laws should help resolve that issue (e.g. [30, 31, 32]).

The kinetic theory of FENE dumbbells predicts hysteretic behaviour in stress–birefringence curves, and thus does not follow a stress–optic law wherein the stress–optic coefficient would be a function of the configuration tensor alone. This is in qualitative agreement with experimental results and more detailed bead–rod or bead–spring simulations [8, 9, 13]. Recent experimental and numerical work [7, 33] also adds to the credibility of simple non–linear dumbbell models. Thus, although the FENE dumbbell model is very crude (in particular, the distribution of solvent drag along the polymer chain and the coupling of internal configuration modes are ignored), it appears to be a realistic starting point for micro–macro simulations of dilute polymer solutions in complex geometries.

In the Appendix, we show that a suitable selection of the spectrum of finite extensibilities b_i can be made in the multi- b FENE–P model so that the resulting stress response in transient uniaxial extension is essentially identical to that of the (single–mode) FENE dumbbell model. Thus, the multi- b FENE–P model appears to be a very good macroscopic model for describing dilute polymer chains in extensional flows. Interestingly, we show that *small* values of the b_i parameters are needed to have a multi- b FENE–P model fit the response of a single–mode FENE model.

This last remark leads us to comment on the selection of suitable values for the various parameters that appear in the models used in this work. For simplicity, let us distinguish three levels of description, namely, level 1: modeling of chains (e.g. Kramers model), level 2: non-linear dumbbell models, and level 3: closed-form constitutive equation. Obviously, each level of description has a phenomenological character to it that should not be ignored. In view of the approximations and idealizations adopted for going from levels n to $n + 1$, it is not at all obvious to us that the model parameters at level n can be unambiguously related to those at level $n - 1$. For example, due to the Peterlin approximation used to go from levels 2 to 3, interpreting the parameters of the FENE–P model in the framework of the underlying FENE kinetic picture can be misleading, especially so for the maximum extensibility parameter b ([12, 34]). A similar situation arises, in our opinion, when one wishes to relate the parameters of chain models to those of the single–mode FENE dumbbell model. Indeed, concentrating all

interactions between the chain and the solvent at both ends of a dumbbell and neglecting internal configuration effects are also significant approximations that are likely to change the interpretation of the model parameters. In other words, it is not clear to us that a range of physically admissible values for the maximum extensibility parameter b of the FENE dumbbell model at level 2 can be defined strictly and unambiguously in terms of parameters for chain models at level 1, as done e.g. in [9].

In view of the phenomenological character of each level of description, we feel that a valid procedure for estimating the values of the model parameters is to fit experimental rheometrical data, as done e.g. in the vortex growth simulations performed by Purnode and Crochet with the FENE-P or FENE-CR model [35, 36] (yielding in this case rather small values for the maximum extensibility parameter b). Alternatively, one could consider the results obtained at level $n - 1$ or $n - 2$ as the “experimental” data to be fitted at level n .

9 Acknowledgments

This work is supported by the ARC 97/02–210 project, Communauté Française de Belgique, and the Brite/EURAM project MPFLOW CT96–0145. The work of V. Legat is supported by the Belgian Fonds National de la Recherche Scientifique (FNRS). We wish to thank H.C. Öttinger for pointing us to ref. [13]. We wish to thank R.G. Larson and J.M. Wiest for helpful discussions regarding birefringence.

References

- [1] J.E. Matta and R.P. Tytus. Liquid stretching using a falling cylinder. *J. Non-Newtonian Fluid Mech.*, 35:215–229, 1990.
- [2] V. Tirtaatmadja and T. Sridhar. A filament stretching device for measurement of extensional viscosity. *Journal of Rheology*, 37(6):1081–1102, 1993.
- [3] M.J. Solomon and S.J. Muller. The transient extensional behavior of polystyrene-based Boger fluids of varying solvent quality and molecular weight. *Journal of Rheology*, 40(5):837–856, 1996.
- [4] S.H. Spiegelberg and G.H. McKinley. Stress relaxation and elastic decohesion of viscoelastic polymer solutions in extensional flow. *J. Non-Newtonian Fluid Mech.*, 67:49–76, 1996.
- [5] N.V. Orr and T. Sridhar. Stress relaxation in uniaxial extension. *J. Non-Newtonian Fluid Mech.*, 67:77–103, 1996.
- [6] J. Van Niewkoop and M.M.O. Muller von Czernicki. Elongation and subsequent relaxation measurements on dilute polyisobutylene solutions. *J. Non-Newtonian Fluid Mech.*, 67:105–123, 1996.

- [7] M.R.J. Verhoef, B.H.A.A. van den Brule, and M.A. Hulsen. On the modelling of a PIB/PB Boger fluid in extensional flow. *J. Non-Newtonian Fluid Mech.*, in press, 1998.
- [8] P.S. Doyle and E.S.G. Shaqfeh. Dynamic simulation of freely-draining, flexible bead-rod chains. *J. Non-Newtonian Fluid Mech.*, in press, 1998.
- [9] P.S. Doyle, E.S.G. Shaqfeh, G.H. McKinley, and S.H. Spiegelberg. Relaxation of dilute polymer solutions following extensional flow. *J. Non-Newtonian Fluid Mech.*, 76:79–110, 1998.
- [10] S.H. Spiegelberg and G.H. McKinley. Elastic and viscous contributions to stress in extensional rheometry of viscous polymer solutions. In A. Ait-Kadi et al., editor, *Proc. XIIIth Int. Congress of Rheology*, pages 211–212. Quebec City, 1996.
- [11] G. Lielens, P. Halin, I. Jaumain, R. Keunings, and V. Legat. New closure approximations for the kinetic theory of finitely extensible dumbbells. *J. Non-Newtonian Fluid Mech.*, 76:249–279, 1998.
- [12] R. Keunings. On the Peterlin approximation for finitely extensible dumbbells. *J. Non-Newtonian Fluid Mech.*, 68:85–100, 1997.
- [13] J.M. Wiest. Birefringence in strong flows of dilute polymer solutions. *Submitted for publication in J. Rheol.*, 1998.
- [14] R.B. Bird, C.F. Curtiss, R.C. Armstrong, and O. Hassager. *Dynamics of Polymeric Liquids, Vol.2, Kinetic theory*. Wiley-Interscience, New York, 2nd edition 1987.
- [15] H.C. Öttinger. *Stochastic Processes in Polymeric Fluids: Tools and Examples for Developing Simulation Algorithms*. Springer, Berlin, 1996.
- [16] M.D. Chilcott and J.M. Rallison. Creeping flow of dilute polymer solutions past cylinders and spheres. *J. Non-Newtonian Fluid Mech.*, 29:381–432, 1988.
- [17] M. Herrchen and H.C. Öttinger. A detailed comparison of various FENE dumbbell models. *J. Non-Newtonian Fluid Mech.*, 68:17–42, 1997.
- [18] G. Lielens, R. Keunings, and V. Legat. Evaluation of the FENE-L model in three-dimensional flow fields. In preparation.
- [19] L. E. Wedgewood, D. N. Ostrov, and R. B. Bird. A finitely extensible bead-spring chain model for dilute polymer solutions. *J. Non-Newtonian Fluid Mech.*, 40:119–139, 1991, and 48:211–211, 1993.
- [20] S.H. Spiegelberg, D.C. Ables, and G.H. McKinley. The role of end-effects on measurements of extensional viscosity in filament stretching rheometers. *J. Non-Newtonian Fluid Mech.*, 64:229–267, 1996.

- [21] R. Sizaire and V. Legat. Finite element simulation of a filament stretching extensional rheometer. *J. Non-Newtonian Fluid Mech.*, 71:89–107, 1997.
- [22] M.I. Kolte, Rasmussen H.K., and O. Hassager. Transient filament stretching rheometer. 2. Numerical simulation. *Rheol. Acta*, 36:285–302, 1997.
- [23] M. Yao and G.H. McKinley. Numerical simulation of extensional deformations of viscoelastic liquid bridges in filament stretching devices. *J. Non-Newtonian Fluid Mech.*, 74:47–88, 1998.
- [24] R. Sizaire. *Numerical study of free-surface Newtonian and viscoelastic flows*. PhD thesis, Université catholique de Louvain, Belgium, 1998.
- [25] P.J. Flory. *Statistical Mechanics of Chain Molecules*. John Wiley, New York, 1969.
- [26] M. Doi and S.F. Edwards. *The Theory of Polymer Dynamics*. Oxford Univ. Press, New York, 1986.
- [27] R.G. Larson. *Constitutive Equations for Polymer Melts and Solutions*. Butterworths, Boston, 1988.
- [28] P.G. de Gennes. Molecular individualism. *Science*, 276:1999, 1997.
- [29] R.G. Larson. Brownian dynamics simulations of a DNA molecule in an extensional flow field. *Submitted for publication in J. Rheol.*, 1998.
- [30] K. Feigl, M. Laso, and H.C. Öttinger. The CONNFFESSIT approach for solving a two-dimensional viscoelastic fluid problem. *Macromolecules*, 28:3261–3274, 1995.
- [31] M.A. Hulsen, A.P.G. van Heel, and B.H.A.A. van den Brule. Simulation of viscoelastic flows using Brownian configuration fields. *J. Non-Newtonian Fluid Mech.*, 70:79–101, 1997.
- [32] P. Halin, G. Lielens, R. Keunings, and V. Legat. The Lagrangian Particle Method for macroscopic and micro-macro viscoelastic flow computations. *J. Non-Newtonian Fluid Mech.*, in press, 1998.
- [33] R.G. Larson, T.T. Perkins, D.E. Smith, and S. Chu. Hydrodynamics of a DNA molecule in a flow field. *Phys. Rev. E*, 55(2):1794–1797, 1997.
- [34] A.P.G. van Heel, M.A. Hulsen, and B.H.A.A. van den Brule. On the selection of parameters in the FENE-P model. *J. Non-Newtonian Fluid Mech.*, 75:253–271, 1998.

- [35] B. Purnode and M.J. Crochet. Flows of polymer solutions through contractions. Part 1 : Flows of polyacrylamide solutions through planar contractions. *J. Non-Newtonian Fluid Mech.*, 65:269–289, 1996.
- [36] B. Purnode and M.J. Crochet. Polymer solution characterization with the FENE-P model. *J. Non-Newtonian Fluid Mech.*, 77:1–20, 1998.
- [37] G. Lielens. PhD thesis, Université catholique de Louvain, Belgium, in preparation.

10 Appendix

We wish to show in this Appendix that a suitable selection of the spectrum of finite extensibilities b_i can be made so that the multi- b FENE-P results for the transient elongational viscosity are virtually those obtained with the single-mode FENE dumbbell model in start-up of uniaxial extension followed by relaxation.

Although the result is for the three-dimensional case, its development is based upon a one-dimensional theory where we retain only the x and xx components of all variables of interest; all other components are assumed to vanish identically. The dumbbells are thus aligned with equal probability in the positive or negative x direction, while the effect of the flow is to modify their length. The resulting mathematical problem is scalar; we shall thus drop all reference to the coordinate system (e.g. $\tau_p = \tau_{p,xx}$, $A = A_{xx}$, $Q = Q_x$). For FENE dumbbells with maximum extensibility b , the one-dimensional analog of eqs. (3,4) read

$$\begin{cases} dQ = \left\{ \kappa Q - \frac{1}{2} \frac{Q}{1 - Q^2/\tilde{b}} \right\} dt + dW, \\ \tau_p = \left\langle \frac{QQ}{1 - Q^2/\tilde{b}} \right\rangle_{\psi_Q} - 1. \end{cases} \quad (18)$$

Here, $\langle \cdot \rangle_{\psi_Q}$ is the configuration space average computed with the distribution function $\psi_Q(Q, t)$, i.e.

$$\langle \cdot \rangle_{\psi_Q} = \int_{-\sqrt{\tilde{b}}}^{\sqrt{\tilde{b}}} \cdot \Psi_Q(Q, t) dQ. \quad (19)$$

Now, let us consider a multi- b FENE-P model with a *continuous* spectrum $\psi_{mb}(b)$ of finite extensibilities. The polymer stress is thus given by

$$\tau_p = \left\langle \frac{A(b)}{1 - A(b)/b} \right\rangle_{\psi_{mb}} - 1, \quad (20)$$

where $\langle \cdot \rangle_{\psi_{mb}}$ is a mode average computed with the distribution $\psi_{mb}(b)$ of finite extensibilities. For a given value of b , the configuration $A(b)$ is obtained as solution to the one-dimensional analog of eq. (7):

$$\frac{dA}{dt} = 2\kappa A + 1 - \frac{A}{1 - A/b}. \quad (21)$$

At this point, we wish to show that eqs. (18) and (20,21) are formally very similar. In order to do so, we normalize the FENE connector Q with its maximum extension, i.e.

$$q = \frac{Q}{\sqrt{\tilde{b}}}, \quad (22)$$

For the multi- b FENE-P model, we define a normalized configuration variable $p(b)$ such that

$$p = \sqrt{\frac{A(b)}{b}}. \quad (23)$$

In terms of q and p , the FENE and multi- b FENE-P models read respectively

$$\begin{cases} dq = \left\{ \kappa q - \frac{1}{2} \frac{q}{1 - q^2} \right\} dt + \frac{dW}{\sqrt{\tilde{b}}}, \\ \tau_p = \left\langle \frac{qq}{1 - q^2} \right\rangle_{\tilde{b}\Psi_q} - 1, \end{cases} \quad (24)$$

and

$$\begin{cases} dp = \left\{ \kappa p - \frac{1}{2} \frac{p}{1 - p^2} \right\} dt + \frac{dt}{2 b p}, \\ \tau_p = \left\langle \frac{pp}{1 - p^2} \right\rangle_{b\Psi_{mb}} - 1, \end{cases} \quad (25)$$

with the constraint $\int_0^\infty b\psi_{mb}(b)db = 1$.

The similarity between eqs. (24) and (25) is striking. Formally, the main difference between FENE and multi- b FENE-P is that the stochastic Brownian term of intensity $\frac{dW}{\sqrt{\tilde{b}}}$ in eq. (24) is a deterministic term of magnitude $\frac{dt}{2 b p}$ in eq. (25). Furthermore, if the length distribution ψ_p of the multi- b FENE-P model is defined by

$$\psi_p(p) = \frac{1}{2} \frac{b}{\tilde{b}} \psi_{mb}(b) \left| \frac{dp}{db} \right|^{-1}, \quad (26)$$

then eq. (25)₂ reads

$$\tau_p = \left\langle \frac{pp}{1-p^2} \right\rangle_{\tilde{b}\psi_p} - 1, \quad (27)$$

which is similar to eq. (24)₂.

These considerations lead us to the following statement: by selecting a mode distribution $\psi_{mb}(b)$ such that the *equilibrium* FENE and multi- b FENE-P length distributions coincide, i.e.

$$\psi_p^{eq}(\cdot) = \psi_q^{eq}(\cdot), \quad (28)$$

one should expect (see Section 6 in [11]) that these two models give very similar dynamics of the polymer stress. In view of eq. (26), the constraint (28) yields the following spectrum ψ_{mb} of finite extensibilities [37]:

$$\psi_{mb}(b) = c \frac{b^{(\tilde{b}-2)/2}}{(1+b)^{(\tilde{b}+3)/2}}, \quad (29)$$

where c is a normalization constant such that $\int_0^\infty \psi_{mb}(b)db = 1$. This particular spectrum is illustrated in Fig. 11, for $\tilde{b} = 50$. We shall refer to the multi- b FENE-P model with the spectrum (29) as the FENE-Pb model. Although quite similar, the FENE and FENE-Pb models are of course not equivalent mathematically [37]. It is worth pointing out that the spectrum (29) selected in order to mimic the FENE theory with finite extensibility $\tilde{b} = 50$ exhibits a maximum value around $b = 10$. In the discrete version of the FENE-Pb model, a large number of modes will thus have an extensibility parameter b_i that is significantly *smaller* than \tilde{b} . This shows that small values of the b_i parameters are needed to have a multi- b FENE-P model fit the response of a single-mode FENE model.

We now apply the above ideas to three-dimensional kinematics. We consider a discrete version of the FENE-Pb model, with a number N_m of finite extensibilities b_i . The latter are selected such that [37]

$$\int_{b_i}^{b_{i+1}} \psi_{mb}(b)db = \frac{1}{N_m + 1}, \quad i = 1, 2, \dots, N_m - 1 \quad (30)$$

$$\int_0^{b_1} \psi_{mb}(b)db = \frac{1}{N_m + 1}, \quad \int_{b_{N_m}}^\infty \psi_{mb}(b)db = \frac{1}{N_m + 1},$$

with ψ_{mb} given by (29). As in Section 4, the polymer stress is the sum of the contributions $\tau_p^{(i)}$ of each mode, where $\tau_p^{(i)}$ is computed by means of eq. (7) with $b = b_i$ in eq. (1).

Figure 12 compares the transient elongation viscosity $\bar{\eta}^+$ predicted with FENE and FENE-Pb models in the start-up of uniaxial elongation followed by relaxation.

The velocity gradient is given by eq. (10) with $We = 6$. As the number of modes increases, i.e. $N_m = 5, 10, 30$, and 100 , one indeed observes convergence of the FENE–Pb results to their FENE counterparts. The optimal selection of the spectrum of finite extensibilities depends, however, upon the flow kinematics. For example, the choice (29) which is excellent for uniaxial elongation is not optimal for bi–axial elongation [37].

List of Figures

- 1 Start-up of uniaxial elongation followed by relaxation ($b = 50, We = 6$): evolution of specified strain rate κ_{xx} and strain ϵ_{xx} . Comparison of results for the transient elongational viscosity $\bar{\eta}^+$ and the mean square molecular extension $\text{tr}\langle\mathbf{Q}\mathbf{Q}\rangle$. Thick curve: FENE; thin curve: FENE–L; dashed curve: FENE–P; dash-dotted curve: FENE–CR. For the stress relaxation phase, we also show the single exponential $\exp(-t)$. 22
- 2 Start-up of uniaxial elongation followed by relaxation ($b = 50, We = 6$): transient elongational viscosity $\bar{\eta}^+$ versus mean square molecular extension $\text{tr}\langle\mathbf{Q}\mathbf{Q}\rangle$. Thick curve: FENE; thin curve: FENE–L; dashed curve: FENE–P; dash-dotted curve: FENE–CR. The FENE and FENE–L hysteresis curves are traversed clockwise. The insets show the FENE distribution $\psi(|Q_x|)$ of projected dumbbell length $|Q_x|$ at selected values of time (also defined in Fig. 1). 23
- 3 Start-up of uniaxial elongation followed by relaxation. FENE–P model with a spectrum of finite extensibilities, using $N_m = 20$ modes that are linearly distributed between $b_1 = 3.5$ and $b_{20} = 20000$. Transient elongational viscosity $\bar{\eta}^+$ versus mean square molecular extension $\frac{1}{N_m} \sum_{i=1}^{N_m} \text{tr} \mathbf{A}^{(i)}$. The hysteresis curves are traversed clockwise. . . 24
- 4 Schematic of the filament stretching device. The initial aspect ratio R_0/L_0 is set to 1.75 in the numerical simulation. 25
- 5 Numerical simulation of start-up of elongation in the filament stretching device, using the velocity compensation technique ($\dot{\epsilon} = 1.6$). Transient Trouton ratio $\bar{\eta}_{est}^+/\eta_0$ as a function of Hencky strain ϵ . Results for a single-mode FENE–CR model. 26

6	Numerical simulation of start-up of elongation in the filament stretching device, using the velocity compensation technique ($\dot{\epsilon} = 1.6$). Axial component of the configuration tensor \mathbf{A} and polymer stress τ_p as a function of the radial coordinate, computed at mid-distance between the plates. Results for a single-mode FENE-CR model ($b = 43$). The insets show the distribution ψ of nodal values of A_{zz} in the form of raw histograms. A localized peak means that A_{zz} is essentially uniform over the cross-section.	27
7	Numerical simulation of start-up of elongation followed by relaxation in the filament stretching device, using the velocity compensation technique. Average polymer stress $\langle \tau_p \rangle$ versus average molecular extension $\langle A \rangle$. Results for a single-mode FENE-CR model ($b = 43$). The hysteresis curves are traversed clockwise.	28
8	Illustration of eq.(14) for an arbitrary distribution of individual configurations c^{ind}	29
9	Stress-optic coefficient C versus time for FENE dumbbells in start-up of uniaxial extension followed by relaxation ($b = 4325, We = 6$). . .	30
10	Stress-optic coefficient C versus birefringence Δn for FENE dumbbells in start-up of uniaxial extension followed by relaxation ($b = 4325, We = 6$). The hysteresis curve is traversed counter-clockwise. .	31
11	Continuous spectrum $\psi_{mb}(b)$ that defines the FENE-Pb model for $\tilde{b} = 50$	32
12	Transient elongational viscosity $\bar{\eta}^+$ in start-up of uniaxial extension followed by relaxation ($\tilde{b} = 50, We = 6$). Convergence of FENE-Pb (dashed curves) to FENE (solid curve), with $N_m = 5, 10, 30$, and 100.	33

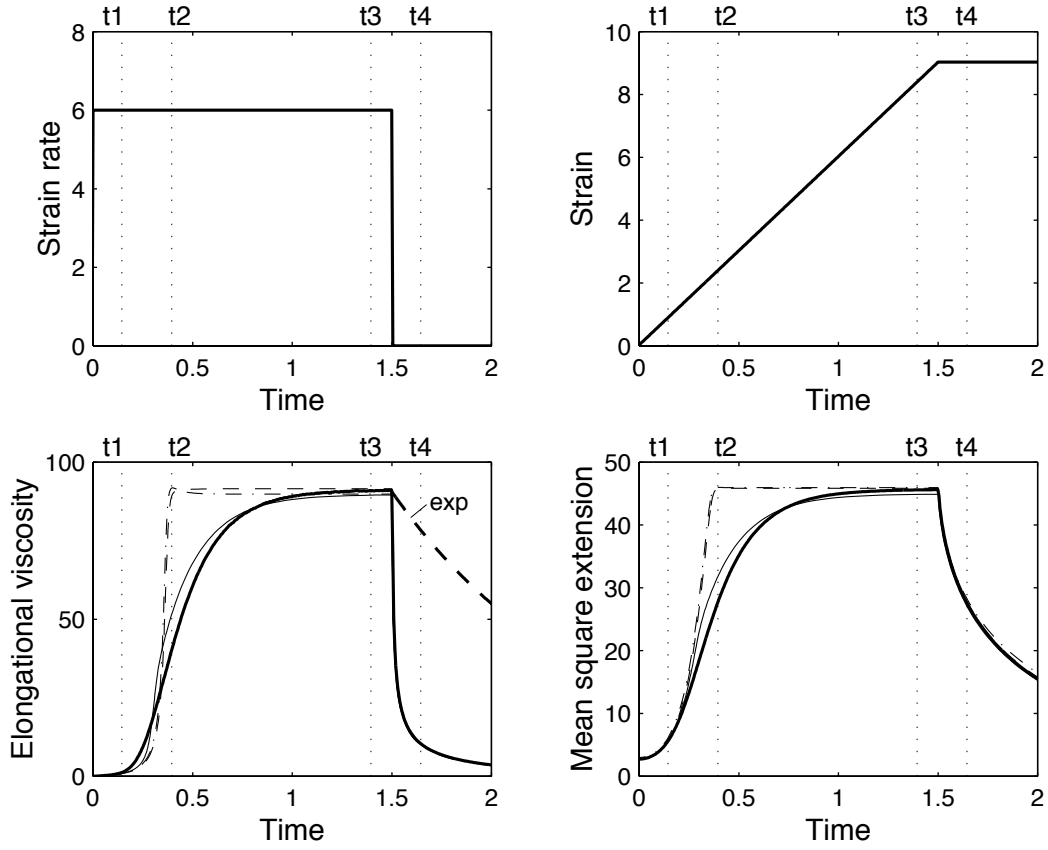


Figure 1: Start-up of uniaxial elongation followed by relaxation ($b = 50$, $We = 6$): evolution of specified strain rate κ_{xx} and strain ϵ_{xx} . Comparison of results for the transient elongational viscosity $\bar{\eta}^+$ and the mean square molecular extension $\text{tr}\langle\mathbf{Q}\mathbf{Q}\rangle$. Thick curve: FENE; thin curve: FENE-L; dashed curve: FENE-P; dash-dotted curve: FENE-CR. For the stress relaxation phase, we also show the single exponential $\exp(-t)$.

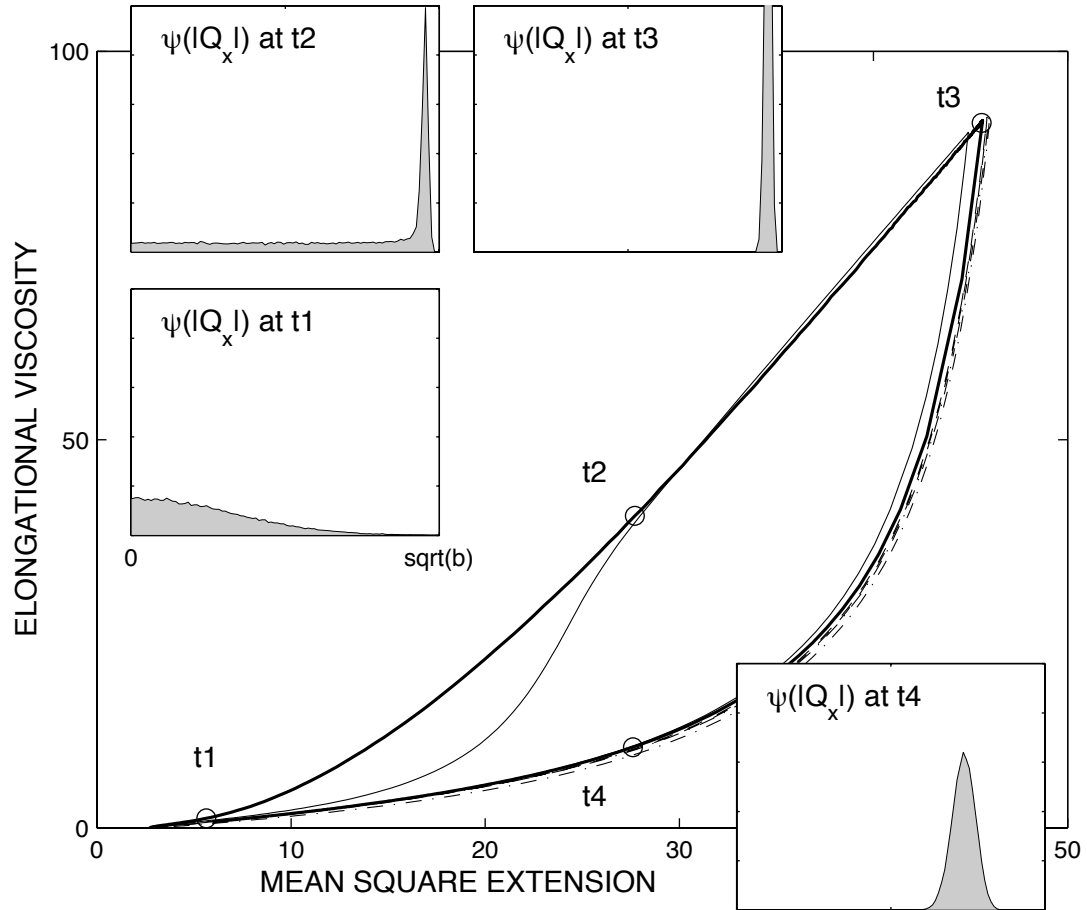


Figure 2: Start-up of uniaxial elongation followed by relaxation ($b = 50$, $We = 6$): transient elongational viscosity $\bar{\eta}^+$ versus mean square molecular extension $\text{tr}\langle\mathbf{Q}\mathbf{Q}\rangle$. Thick curve: FENE; thin curve: FENE-L; dashed curve: FENE-P; dash-dotted curve: FENE-CR. The FENE and FENE-L hysteresis curves are traversed clockwise. The insets show the FENE distribution $\psi(|Q_x|)$ of projected dumbbell length $|Q_x|$ at selected values of time (also defined in Fig. 1).

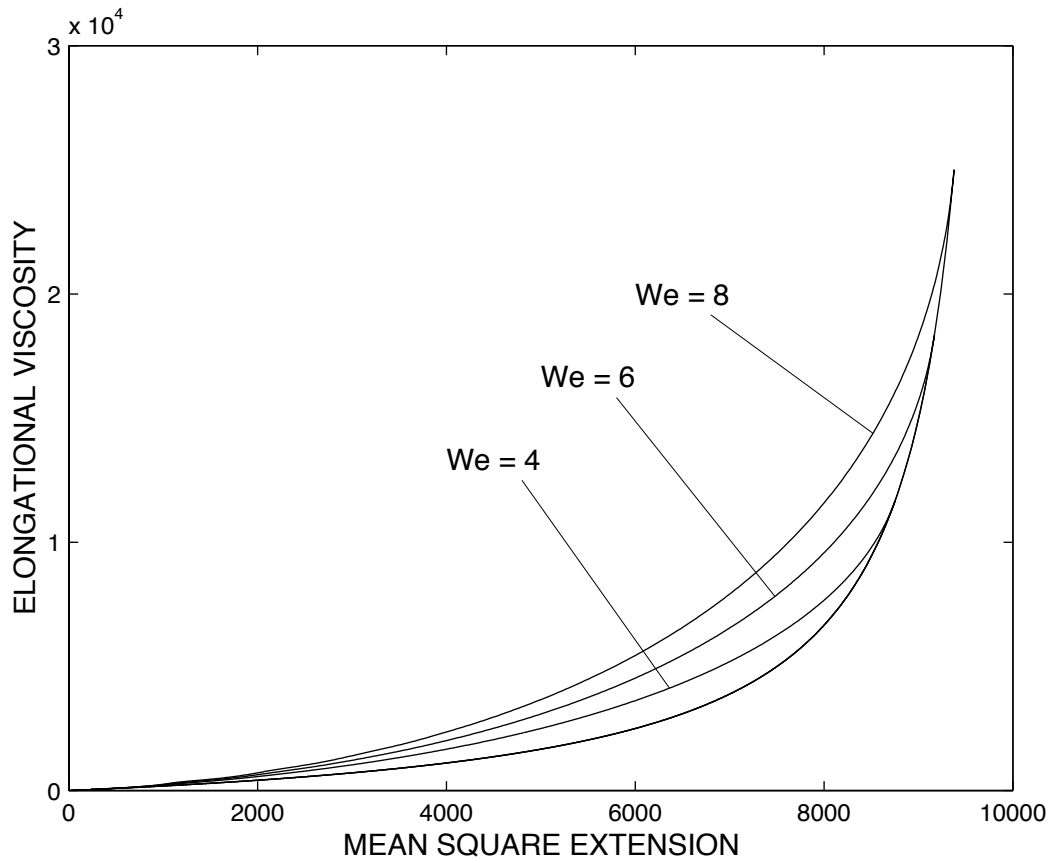


Figure 3: Start-up of uniaxial elongation followed by relaxation. FENE-P model with a spectrum of finite extensibilities, using $N_m = 20$ modes that are linearly distributed between $b_1 = 3.5$ and $b_{20} = 20000$. Transient elongational viscosity $\bar{\eta}^+$ versus mean square molecular extension $\frac{1}{N_m} \sum_{i=1}^{N_m} \text{tr} \mathbf{A}^{(i)}$. The hysteresis curves are traversed clockwise.

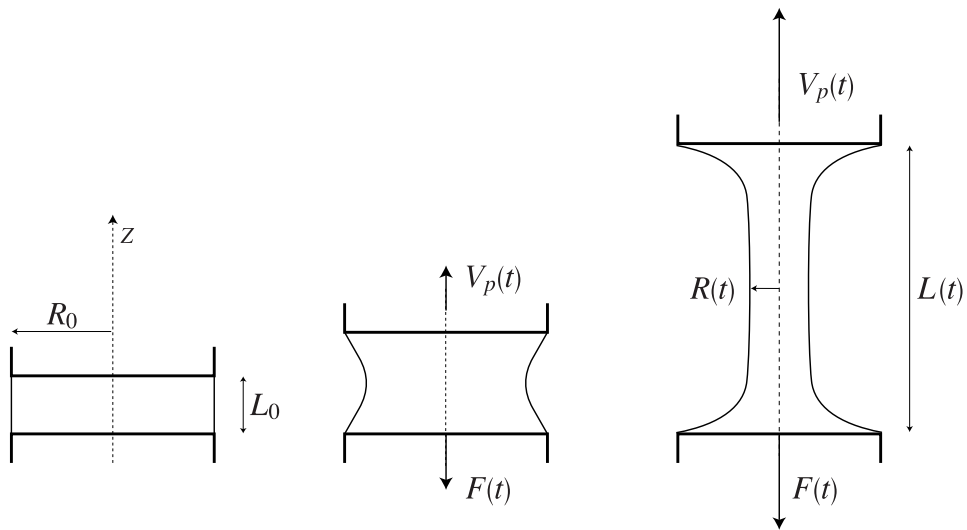


Figure 4: Schematic of the filament stretching device. The initial aspect ratio R_0/L_0 is set to 1.75 in the numerical simulation.

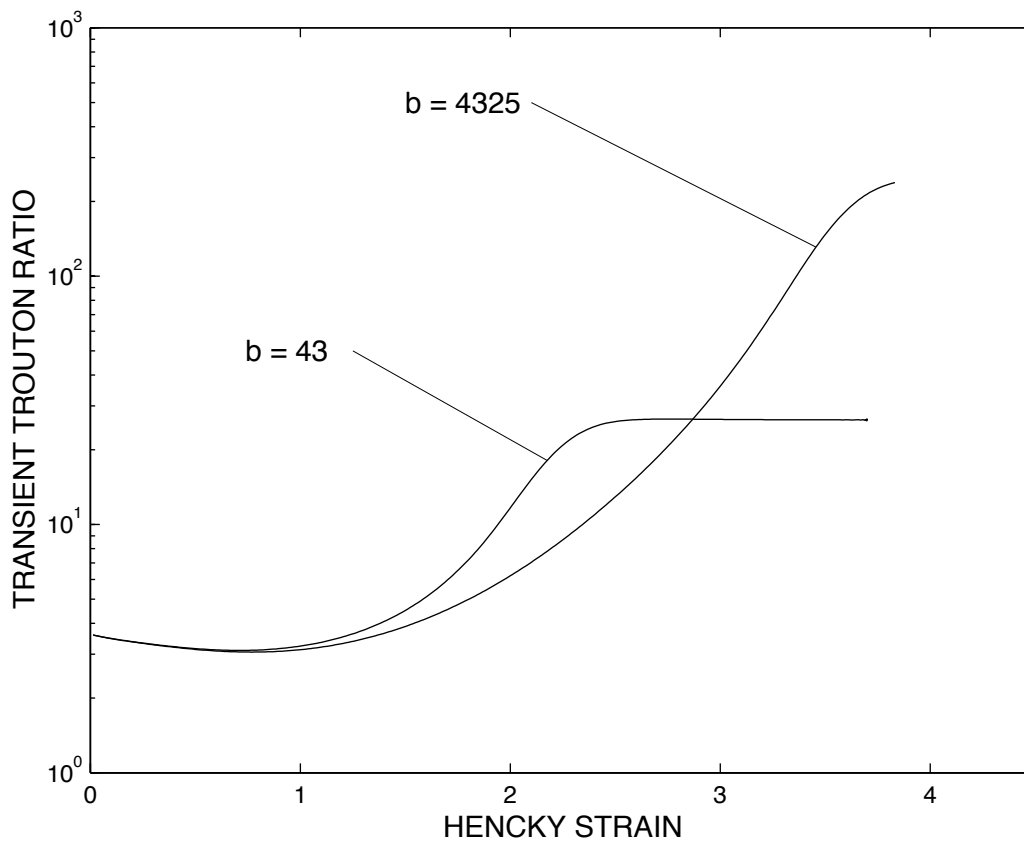


Figure 5: Numerical simulation of start-up of elongation in the filament stretching device, using the velocity compensation technique ($\dot{\varepsilon} = 1.6$). Transient Trouton ratio $\bar{\eta}_{est}^+/\eta_0$ as a function of Hencky strain ε . Results for a single-mode FENE-CR model.

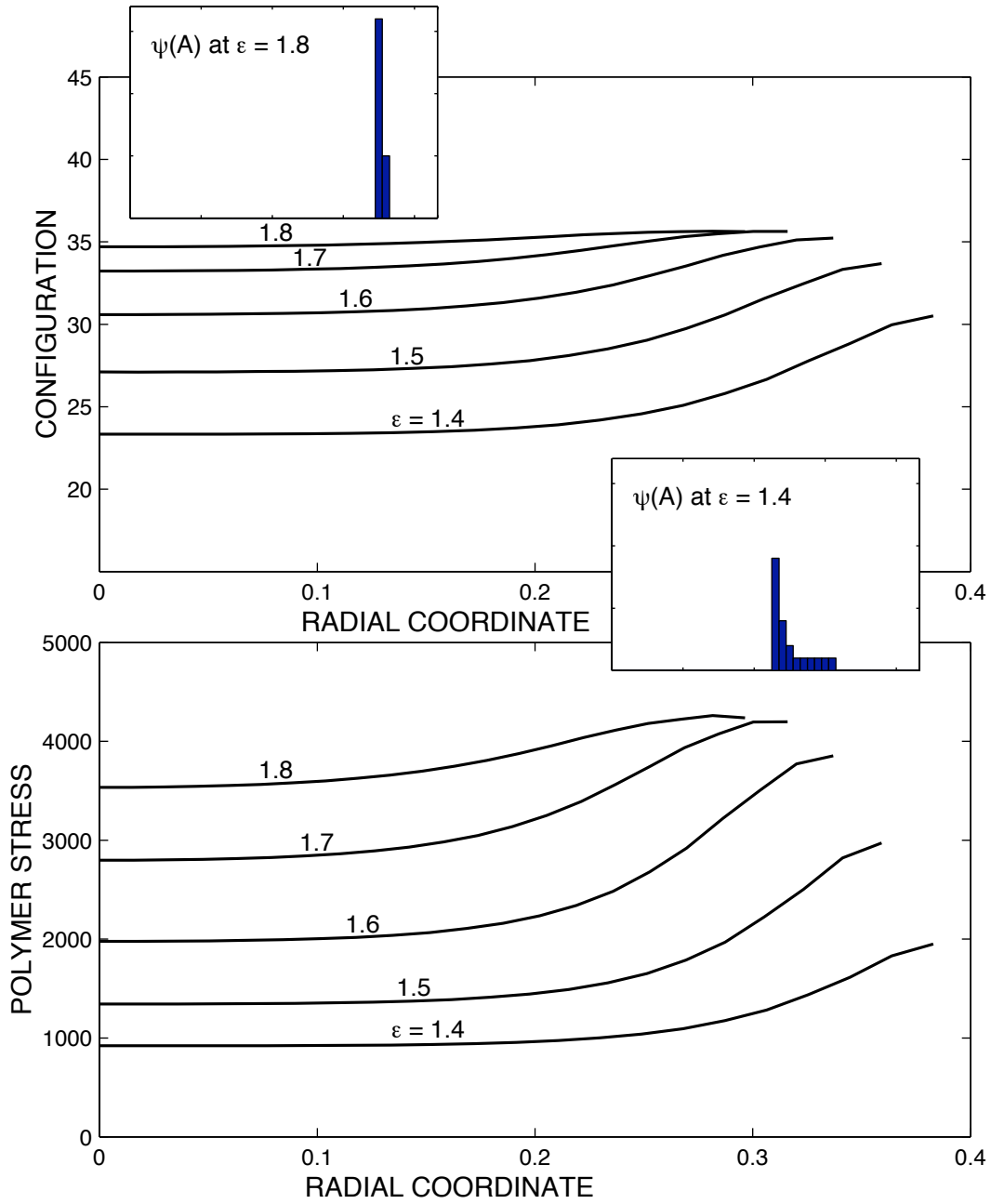


Figure 6: Numerical simulation of start-up of elongation in the filament stretching device, using the velocity compensation technique ($\dot{\varepsilon} = 1.6$). Axial component of the configuration tensor \mathbf{A} and polymer stress τ_p as a function of the radial coordinate, computed at mid-distance between the plates. Results for a single-mode FENE-CR model ($b = 43$). The insets show the distribution ψ of nodal values of A_{zz} in the form of raw histograms. A localized peak means that A_{zz} is essentially uniform over the cross-section.

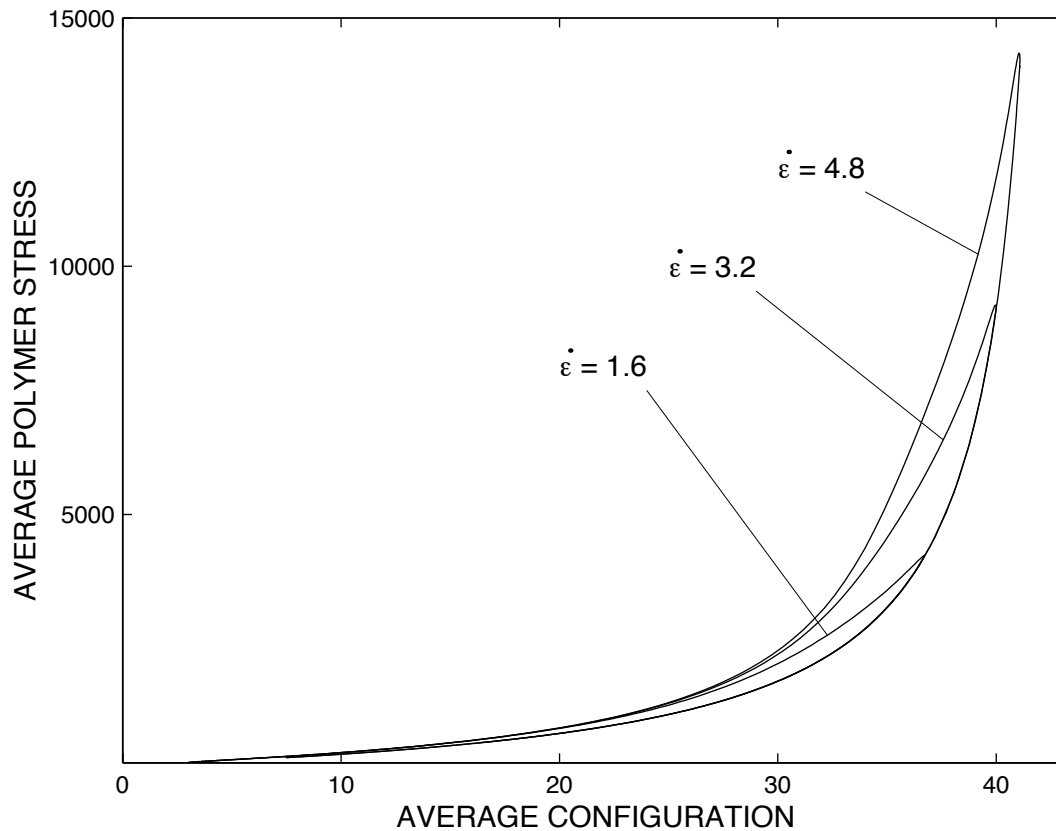


Figure 7: Numerical simulation of start-up of elongation followed by relaxation in the filament stretching device, using the velocity compensation technique. Average polymer stress $\langle \tau_p \rangle$ versus average molecular extension $\langle A \rangle$. Results for a single-mode FENE-CR model ($b = 43$). The hysteresis curves are traversed clockwise.

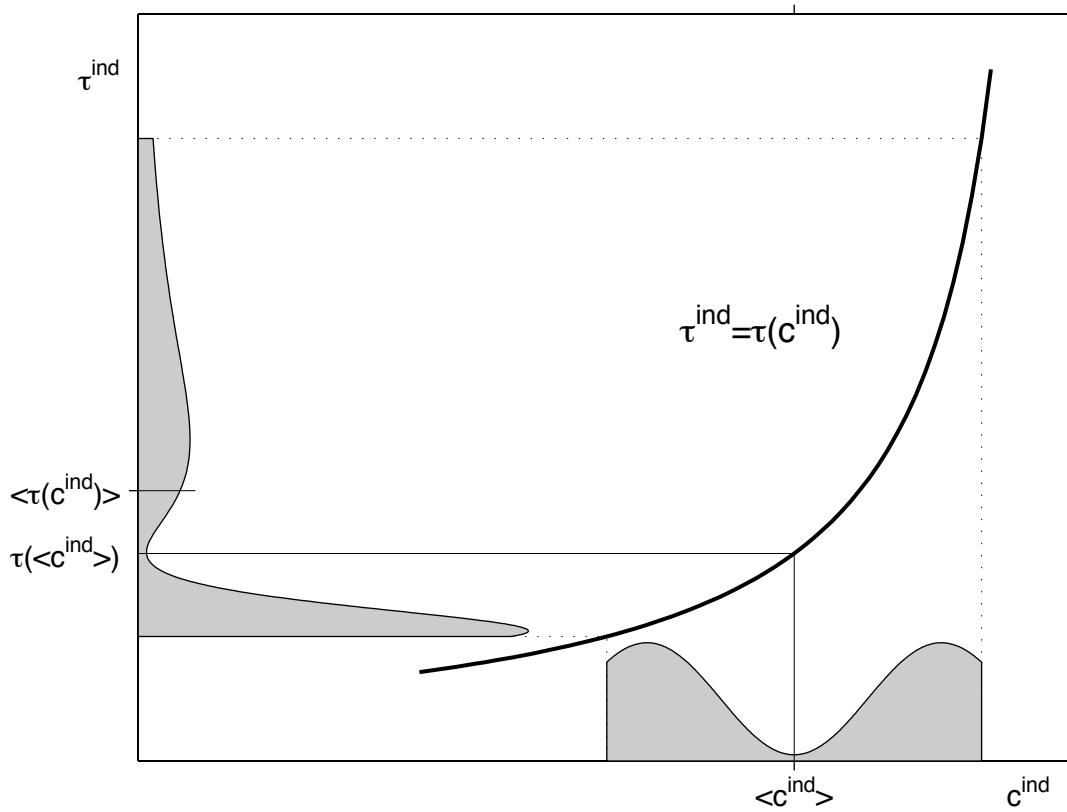


Figure 8: Illustration of eq.(14) for an arbitrary distribution of individual configurations c^{ind} .

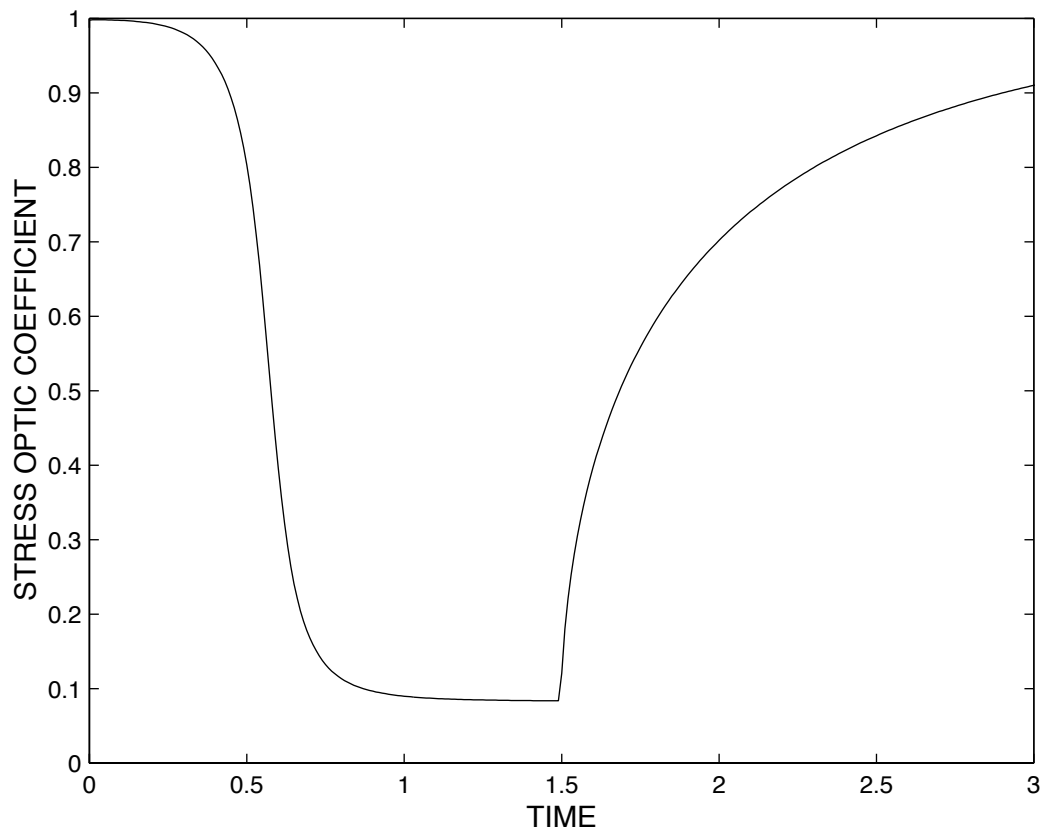


Figure 9: Stress-optic coefficient C versus time for FENE dumbbells in start-up of uniaxial extension followed by relaxation ($b = 4325$, $We = 6$).

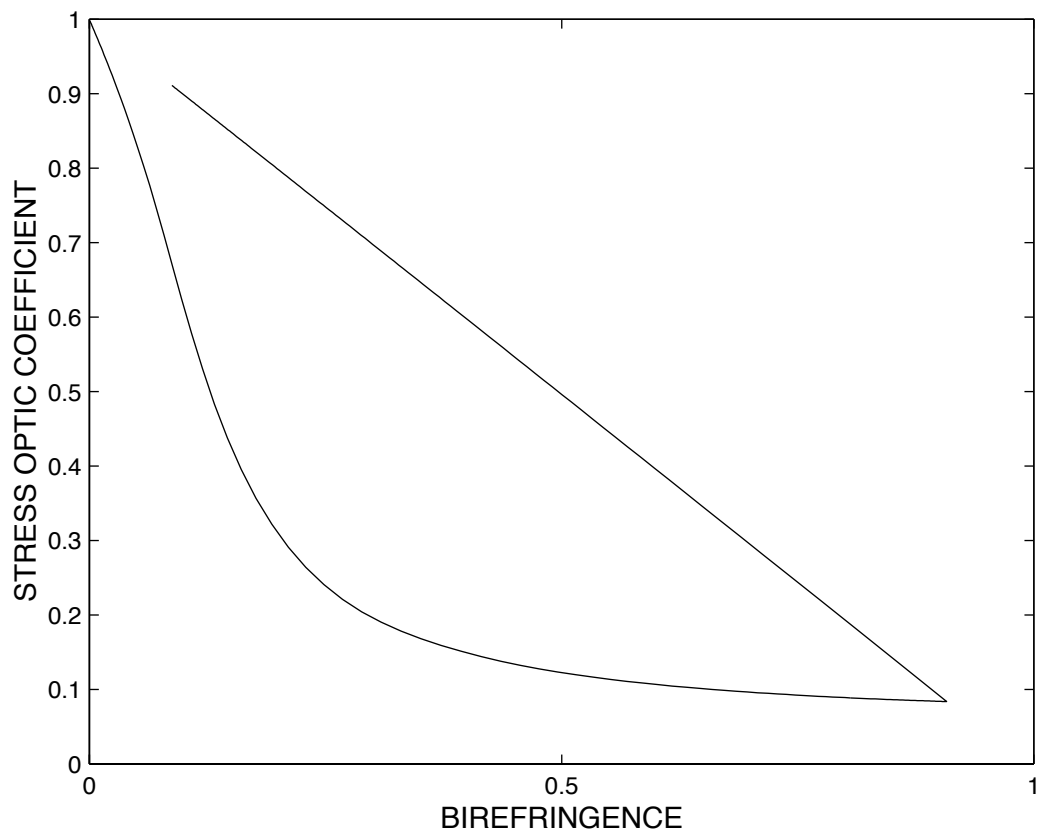


Figure 10: Stress–optic coefficient C versus birefringence Δn for FENE dumbbells in start-up of uniaxial extension followed by relaxation ($b = 4325$, $We = 6$). The hysteresis curve is traversed counter-clockwise.

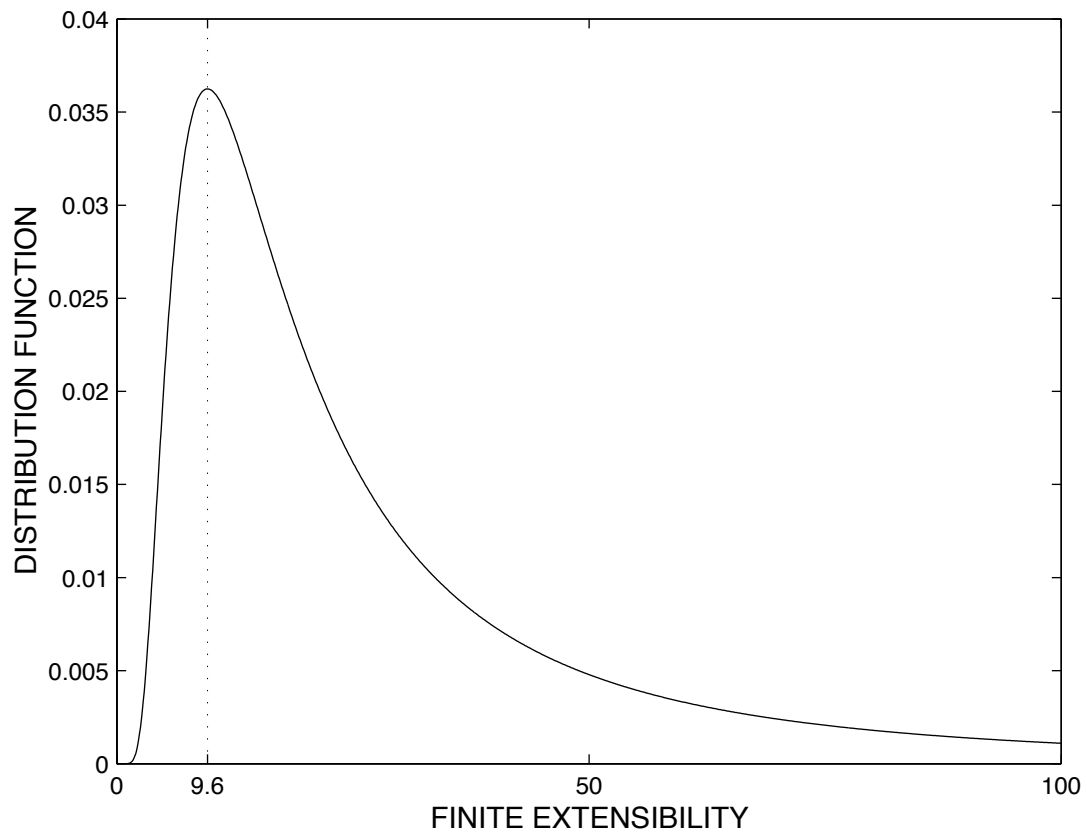


Figure 11: Continuous spectrum $\psi_{mb}(b)$ that defines the FENE-Pb model for $\tilde{b} = 50$.

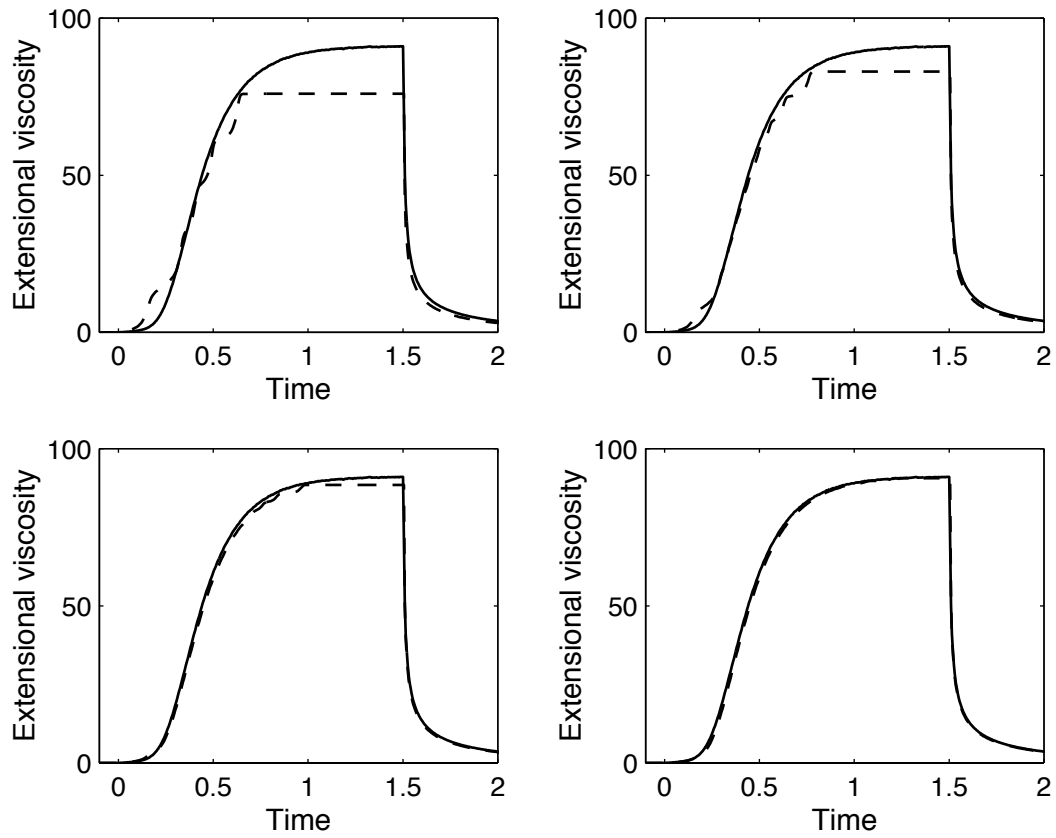


Figure 12: Transient elongational viscosity $\bar{\eta}^+$ in start-up of uniaxial extension followed by relaxation ($\tilde{b} = 50, We = 6$). Convergence of FENE-Pb (dashed curves) to FENE (solid curve), with $N_m = 5, 10, 30,$ and 100 .